Experiments in Fluids manuscript No.
(will be inserted by the editor)

The response of surface buoyancy flux-driven convection to localized mechanical forcing

K.E. Matusik · **S.G. Llewellyn Smith**

Received: date / Accepted: date

Abstract We present laboratory experiments in which both a buoyancy and mechanical forcing are imposed on the surface of a rectangular tank filled with freshwater. The buoyancy forcing is generated by a saltwater source at the surface that drives a sinking half-line plume along one endwall, and the mechanical forcing is generated by a continuous flow of freshwater across the surface of the tank. A steady-state circulation is achieved when the advection of salt by the plume is matched by the diffusion of salt through the upper boundary. The surface stress drives flow in the same direction as the plume, resulting in a convective cell whose depth is determined by the interplay of the two forcings. When the surface stress is relatively weak, the steady-state flow is described by a high-Rayleigh number 'recycling box' model for horizontal convection (Hughes et al, 2007). Once the stress is strong enough to overturn the stratified waters, a region of localized mixing develops. The immediate consequence of this regional turbulence is a net input of stabilizing buoyancy in the form of fresher water into the plume, which renders it too weak to penetrate to the bottom boundary. Generally, the plume is unable to recover a full-depth circulation within the experiment time frame. The resulting flow can be described by the recycling box model with a spatially-varying turbulent diffusivity parameterized by the characteristics of the turbulent eddy that develops in the mixing region. The results of this work apply experimental techniques to show that, with adequate mechanical forcing, a buoyancy-driven circulation will develop localized mixing that significantly alters the overall structure and density distribution of the circulation for relatively long timescales. The experimental results also corroborate the recycling box model as a valid descriptor of the flow structure in such systems.

This work was funded by National Science Foundation awards OCE-0926481 and OCE-1259580.

K.E. Matusik
Department of Mechanical and Aerospace Engineering, Jacobs School of Engineering, UCSD, 9500 Gilman Drive, La Jolla, CA 92093-0411, USA
E-mail: kmatusik@anl.gov
Present address: Energy Systems Division, Argonne National Laboratory, 9700 South Cass Avenue, Lemont, IL 60439, USA

S.G. Llewellyn Smith
Department of Mechanical and Aerospace Engineering, Jacobs School of Engineering and Scripps Institution of Oceanography, UCSD, 9500 Gilman Drive, La Jolla, CA 92093-0411, USA

Keywords Horizontal convection · Buoyancy-driven convection · Surface stress · Turbulent mixing · Particle image velocimetry · Synthetic schlieren

1 Introduction

A number of coupled atmosphere-ocean processes are responsible for maintaining the globally stable stratification of the earth's oceans, as well as driving a deep meridional overturning circulation (MOC) (Wunsch, 2005). The main drivers of this circulation are thought to be surface buoyancy fluxes (e.g. Hughes and Griffiths, 2006) and surface wind stress (e.g. Toggweiler and Samuels, 1997). The former drive a flow by setting up pressure gradients due to horizontal variations in density. The latter establish zones in which Ekman transport brings dense waters from below to the ocean surface. Various other processes also contribute to maintaining the MOC, primarily by inducing diapycnal mixing (Wunsch and Ferrari, 2004). Surface and internal gravity waves triggered by atmospheric winds and tides, as well as topography, result in localized regions of turbulence, as well as transport of energy over large distances (Ledwell, 2017; McDougall and Ferrari, 2018). It has also been theorized that the biosphere plays an active role in enhancing mixing (Dewar et al, 2006). Nevertheless, it is the interplay between wind-driven upwelling and surface buoyancy fluxes that primarily results in the mean MOC and the corresponding stratification in the oceans, with density transport enhanced through mixing processes.

The MOC not only sets the stratification and distribution of both heat and water masses in the oceans, but also controls the global redistribution and storage of chemical species, like carbon dioxide (Kuhlbrodt et al, 2007). As such, the MOC plays a central role in the earth's climate (Schmittner, 2005; Vellinga and Wood, 2002). The current study is inspired by the two dominant drivers of the MOC, and more specifically by a desire to better understand the interaction between a mechanical and buoyancy forcing acting simultaneously on a system. To this end, we explore experimentally a simple two-dimensional (2D) non-rotating model of convection maintained by surface buoyancy and mechanical forcings. The buoyancy forcing is created by injection of a salty plume at the surface of a volume of freshwater. The imposed mechanical forcing on the upper boundary is in the form of a constant shear stress, created by a steady throughput of freshwater along the surface. An overview of surface buoyancy-driven convection and related work, as well as relevant scaling laws, is presented in Sect. 2. In the oceans, a zonal wind stress drives a meridional Ekman flow because of the Earth's rotation. While the full effects of Ekman transport cannot be simulated without including the Coriolis force, for experimental simplicity, we consider only the component of the transport that acts in the same direction as the buoyancy-driven circulation. Thus, for the experiments discussed in Sect. 3, a surface stress is imposed parallel to the buoyancy gradient to simulate convection coupled with mechanical forcing along the surface layer. Qualitative and quantitative results of the experiments are presented in Sect. 4, and an overview of the system's adjustment toward equilibrium in Sect. 5. Equations describing the "recycling box" model of Hughes et al (2007) are given in Sect. 6, as well as a comparison of theory and experiment. Further discussion is presented in Sect. 7. Finally, we conclude in Sect. 8, offering potential implications of the current results on large bodies of water subject to surface mechanical forcing over timescales that are on the order of the timescale of the system's natural response.

2 Background

The overturning circulation that results from a differential buoyancy flux imposed along a horizontal boundary is referred to as "horizontal convection" (Hughes and Griffiths, 2008). The study of this flow is largely motivated by its relevance to the global ocean circulation, as in the pioneering work of Sandström (1908) and Rossby (1965), among others. Along with its relevance to the MOC, horizontal convection may also be exploited in industrial applications, such as modulating temperature conditions in buildings (Linden, 1999), as well as optimizing the large-scale manufacture of glass (Chiu-Webster et al, 2008).

2.1 Governing Parameters & Equations

The relevant parameters describing the steady-state circulation maintained by a horizontal buoyancy flux include the flux Rayleigh number,

$$Ra_B = \frac{BL^3}{\nu\kappa^2}, \tag{1}$$

the aspect ratio,

$$A = \frac{H}{L}, \tag{2}$$

and the Prandtl number (or the analogous Schmidt number for a solute),

$$Pr = \frac{\nu}{\kappa} = \sigma, \tag{3}$$

where B $(\mathrm{m}^3\mathrm{s}^{-3})$ is the imposed rate of supply of specific buoyancy per unit box width, H and L are the box height and length, respectively, ν is the kinematic viscosity of the fluid, and κ is the diffusivity of the stratifying species (Hughes and Griffiths, 2008). The vorticity and density equations describing the 2D, steady-state flow in the Boussinesq approximation are

$$\frac{\partial(\psi,\nabla^2\psi)}{\partial(x,z)} - \nu\nabla^4\psi - \frac{\partial b}{\partial x} = 0, \tag{4}$$

$$\frac{\partial\psi}{\partial x}\frac{\partial b}{\partial z} - \frac{\partial\psi}{\partial z}\frac{\partial b}{\partial x} = \kappa\nabla^2 b, \tag{5}$$

where the streamfunction ψ is related to the velocity by $(u,w) = (-\partial\psi/\partial z, \partial\psi/\partial x)$ and the buoyancy, b, is defined as $b = g(\rho_0-\rho)/\rho_0$ where ρ is the density and ρ_0 is a reference density. In the boundary layer, scaling arguments reveal that the main balance in eqn. (4) is between the diffusion and buoyancy terms, for large Pr (Rossby, 1965). Thus, diffusion of the stratifying species through the boundary layer is balanced by buoyancy-driven advection of fluid. The mechanism of diffusion is essential in achieving a steady-state circulation; if it were neglected, the tank would fill up with dense fluid as per the filling-box model (Baines and Turner, 1969), since there would be no mechanism by which to transfer buoyancy out of the volume. Inside the boundary layer, vertical variations in the flow dominate those in the horizontal, resulting in the boundary layer thickness scaling (Rossby, 1965; Mullarney et al, 2004),

$$\frac{\delta_{bl}}{L} \sim Ra_B^{-1/6}. \tag{6}$$

The volume transport per unit spanwise width, ψ_{bl}, then scales as

$$\frac{\psi_{bl}}{\kappa} \sim Ra_B^{1/6}. \tag{7}$$

The boundary layer scalings given in eqns. (6) and (7), first derived by Rossby (1965), are valid for large Pr and $A \sim O(1)$, and have been confirmed with experimental and numerical work (e.g. Mullarney et al, 2004; Rossby, 1998; Beardsley and Festa, 1972).

Hughes et al (2007) derive similar scalings by considering the inviscid filling-box model of Baines and Turner (1969) which describes a destabilizing buoyancy source in a confined space with a sink of buoyancy located on the same boundary. The addition of a sink to remove buoyancy at an equal rate at which it is supplied requires the advection of the interior density field to be balanced everywhere by vertical diffusion of the stratifying species out of the volume. The theoretical framework used to describe the results of the present set of experiments makes use of this recycling box model.

If a stress is imposed on the surface of the fluid, an additional scaling arises for the streamfunction,

$$\psi_{bl} \sim \frac{\tau_{max}\delta_{bl}^2}{\nu}, \tag{8}$$

where τ_{max} $(\mathrm{m^2 s^{-2}})$ is the maximum surface stress. Combining eqn. (8) with the Rossby scaling for the streamfunction and boundary layer thickness, a nondimensional parameter may be constructed that embodies the relationship between mechanical and buoyancy forcing (Hazewinkel et al, 2012),

$$S_{\delta f} = \frac{\sigma S}{Ra_B^{1/2}} \quad \text{where} \quad S = \frac{\tau_{max} L^2}{\nu^2}. \tag{9}$$

Here, S is a measure of the strength of the surface mechanical forcing. If $S_{\delta f} \gg 1$, the circulation is expected to be mechanically-driven, while if $S_{\delta f} \ll 1$, the flow is buoyancy-driven; the present experiments explore the limiting case of $S_{\delta f} \sim O(1)$.

2.2 Related Work

Recent laboratory experiments that explore horizontal convection forced by differential heating at a boundary (e.g. Rossby, 1965; Mullarney et al, 2004; Wang and Huang, 2005) all exhibit similar qualitative flow features. Specifically, a boundary layer develops adjacent to the boundary at which the convection is forced. A narrow vertical plume located against the endwall transports the boundary layer fluid down the full depth of the tank, subsequently ejecting it into the interior to form a relatively weak and broad vertical outflow toward the forcing boundary. The steady-state convective cell is highly asymmetric as the advecting plume is much more efficient than diffusion in transporting density anomalies (Paparella and Young, 2002). The bulk stratification is stable, albeit much weaker than that in the boundary layer. In addition, the plume is turbulent for $Ra_B > 10^{12}$ (Mullarney et al, 2004). Similar flow characteristics have been observed in numerical simulations for Ra near $O(10^8)$, where Ra is defined based on a horizontal temperature difference (e.g. Beardsley and Festa, 1972; Rossby, 1998; Mullarney et al, 2004; Paparella and Young, 2002), and more recently for higher Ra regimes (e.g. Gayen et al, 2012, 2014).

The majority of laboratory experiments simulating horizontal convection have been carried out with heat as the stratifying species, where either a gradient profile (e.g. piecewise,

linear, etc.) of constant temperature, heat flux, or hybrid thereof, is imposed at a single horizontal boundary. With water as the working fluid, using heat to drive the circulation gives a Pr of $O(1)$, a value relevant to the oceans. Heat also has the benefit of not introducing spurious dynamics that may arise when a sink is added to the experiment setup for the purpose of maintaining zero net volume flux. Moreover, due to the larger diffusion coefficient of heat, these experiments may be run for the full length of time required for molecular diffusion to act on the whole domain, $\tau_H = H^2\kappa^{-1}$, which ensures that the system has reached an equilibrated state. This timescale is unreachable when a stratifying species such as salt is used to generate the buoyancy flux, for which $\tau_H \sim O(5)$ years, contingent on the experiment geometry. However, saltwater experiments have other advantages in the laboratory, namely that they are easier to insulate, and allow access to higher Ra_B and Pr (or the analogous Schmidt number) regimes due to the smaller mass diffusivity of salt in comparison to the thermal diffusivity of heat. Indeed, convection experiments driven by solutal buoyancy fluxes have been previously carried out by Pierce and Rhines (1996) and Whitehead and Wang (2008). However, because the density of the fluid exiting the tank must be at the mean density of the saline and freshwater sources when the flow has reached a steady state, such experiments tend to impose constraints on the density field near the sink region.

More recent experimental work by Stewart et al (2012) examines the overturning circulation maintained by a solutal surface buoyancy forcing in the presence of turbulent mixing. The experiment setup rectifies the challenge of imposing a mean density condition at an arbitrary level in the tank by instead imposing a boundary condition of freshwater on the upper surface, which is free to adjust accordingly to the solute-driven circulation. The vertical transport of salt into this freshwater layer must equal the salt input into the tank and the salinity is only imposed at the source, where it is set by the plume, and at the surface, where it is set by the freshwater layer and therefore equal to 0. The experimental design described in this paper is based on the setup pioneered in Stewart et al (2012). It should be noted that this class of experiments deviates from the model of pure horizontal convection in that it requires a volume source and corresponding sink in the flow to establish a zero net volume flux, and places buoyancy flux constraints on the system. However, experiments show both qualitative and quantitative similarities between solutal surface buoyancy-driven and thermally-driven convection models, justifying the usefulness of such experiments.

Some numerical work has investigated the effects of an imposed surface stress on horizontal convection. Beardsley and Festa (1972) numerically solved horizontal convection forced by a non-uniform temperature difference and an opposing constant stress for $Ra \sim O(10^4)$, where Ra is based on a horizontal temperature difference. The authors reported the development of a two-cell structure in steady state. Ilicak and Vallis (2012) studied a non-hydrostatic Boussinesq model, where the stress was achieved via a periodic vorticity field on the surface. The authors found that with increased stress, the boundary layer deepened considerably and the maximum streamfunction increased relative to the zero-stress case. Hazewinkel et al (2012) considered a 2D non-rotating Boussinesq fluid subject to a monotonically decreasing surface buoyancy forcing and a sinusoidal surface stress. The stress drove a circulation in the opposite direction to the clockwise circulation forced by the buoyancy. Numerical simulations up to $Ra \sim O(10^8)$ revealed the existence of a competitive forcing regime where a two-cell circulation developed: a shallow, mechanically-driven cell, and a deeper, buoyancy-driven cell. The authors assess that in order for the surface stress to be competitive with buoyancy forcing, its magnitude must be comparable to the stress across Rossby's boundary layer in the purely buoyancy-driven flow, thus arriving at the scaling in eqn. (9). To date, no experimental work that explores the resulting flow features of a cou-

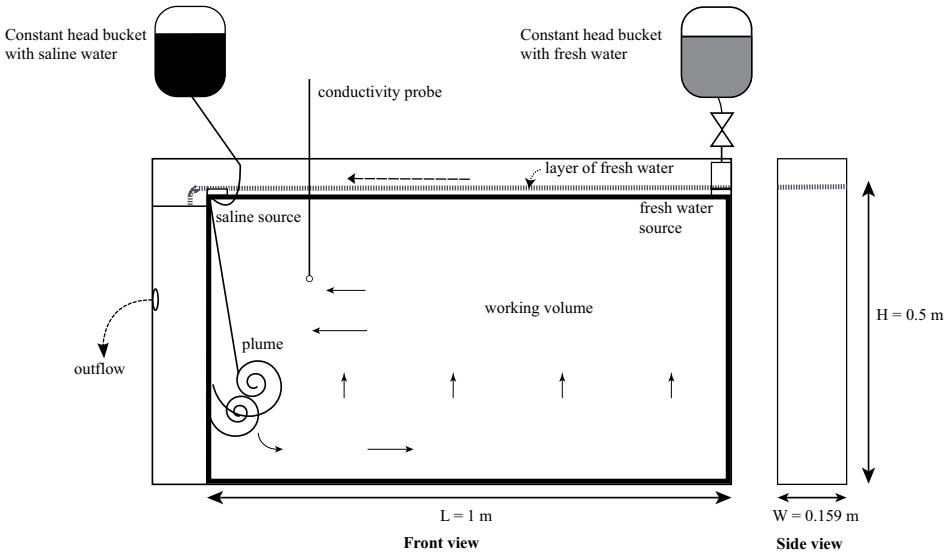

Fig. 1: Front and side views of the experiment setup. The working volume corresponds to the area outlined by the rectangular box of heavier line weight. Arrows indicate the direction of buoyancy-driven flow.

pled surface stress and buoyancy flux-driven system, in either the case where the two drivers work parallel or antiparallel to each other on the circulation, has been reported.

3 Experiments

3.1 Apparatus

The experiment setup is based on the work of Stewart et al (2012) and is pictured in Figure 1. An acrylic tank with inner dimensions of $1.2 \times 0.159 \times 0.6$ m^3 ($L \times W \times H$) was used for all experiments. In order to maintain a zero net flux of volume, a spillway was installed on the left-hand side of the tank. The dimensions of the working volume, taken to be to the right of the vertical partition that separates the spillway from the experiment, were L = 1.0 m and H = 0.5 m, giving an aspect ratio, A, of 0.5.

Fresh de-ionized water at $\rho_f = 998$ kg m^{-3} was fed into the tank from a constant head bucket through a polystyrene container that was fitted with a porous base, ensuring that the water entered the tank uniformly in the spanwise direction and with negligible momentum. A needle valve downstream of the constant head bucket allowed adjustment of the flow rate of freshwater per spanwise width, Q_f, into the tank.

Saline water (varied between ρ_d =1010–1030 kg m^{-3}) was likewise pumped into a constant head bucket before entering the tank at a fixed volume flux per unit width of $Q_d = 16.8$ mm^{2}s^{-1}. The salt water was prepared a day in advance by mixing de-ionized water and high-grade evaporated salt in a plastic drum. The source tubing was positioned so that the dense water was directed into the bottom corner of an acrylic plate inside the tank, causing the inflow to spread out into a full-width line source with negligible momentum

flux. The acrylic plate also prohibited any dense water from escaping into the overflow. The dense water source formed a sinking, fully turbulent endwall half-plume on the left-hand side of the tank, which gave rise to a buoyancy-driven counter-clockwise circulation.

All experiments were performed with room temperature held constant at $22 \pm 1^{\circ}$C. To inhibit any temperature fluctuations, the experiment tank sat on 10 cm of polystyrene insulation, and was covered with 38 mm of polystyrene insulation on all sides (excluding the surface) when data were not being recorded. In order to ensure that the density field was not affected by temperature fluctuations, two thermocouples logged the temperature in the tank, with one stationed 10 cm below the water surface on the right, and the other in the bottom left corner; a third thermocouple was used to record the ambient temperature of the room. Temperature profiles were recorded at 100 mHz for the full duration of each experiment.

The synthetic schlieren technique was used to obtain 2D quantitative density field maps of the flow (Dalziel Research Partners, 2008) using a mask of randomly distributed dots of 1 mm diameter. Because the method is highly sensitive to thermal noise, black tarp shielded the area between the camera and tank in order to block out convection induced by laboratory ventilation as well as the heat generated from electronic sources. Images were recorded using a progressive scan charge-coupled device (CCD) camera with a sensor size 1392 $\times$ 1040 px (H $\times$ V) and a pixel size of 6.46 μm. The camera was fitted with a manual zoom video lens, providing a final pixel resolution of 0.83 mm.

The density profile of the thin boundary layer near the surface could not be resolved using the current synthetic schlieren setup due to resolution limitations on the camera. In order to resolve the boundary layer, a conductivity probe was installed 28 cm from the left-hand side of the spillway, and 5 cm from the front of the tank. The response time of the probe is $<$ 200 ms, with an output resolution of approximately 4 mV (Kanda, 2002), or 50 μg cm^{-3} in terms of fluid density. The conductivity probe was mounted on a vertical translation stage. In order to acquire a voltage signal from the conductivity probe, a small volume of fluid had to be continuously siphoned through the inner tube. The pumping rate was set to approximately 36 mm^3 s^{-1}, a flow rate small enough to have no apparent effect on the circulation. The probe traversed at an approximate speed of 0.10 mm s^{-1} with a maximum penetration depth of 23 cm from the surface, allowing almost half of the working volume to be profiled.

An Nd:YAG laser was used for particle image velocimetry (PIV). The seeding particles were silver-coated hollow glass spheres with an average diameter of 13 μm and average density of 1600 kg m^{-3}. The Stokes number of the tracer particles is $O(10^{-5})$, hence they are expected to faithfully follow the flow field. The camera used for recording PIV images was an Imager Compact with a 1360 $\times$ 1024 px (H $\times$ V) HighRes CCD sensor and pixel size of 4.65 μm. The camera was fitted with a manual zoom lens, providing a final pixel size of 0.76 mm. To create the desired laser sheet size, the beam first passed through a compound lens designed to reduce its diameter, followed by a set of plano-concave and plano-convex lenses to place the focal point at the midpoint of the tank. The beam then passed through a 30° full fan angle laser line generator lens in order to create the laser sheet at the required height. The thickness of the sheet at the midpoint of the tank was 0.32 mm, with a maximum thickness of 1 mm at the edges.

Finally, for flow visualization, potassium permanganate ($KMnO_4$) was used to dye the dense water after all measurements were recorded.

3.2 Mechanical forcing

The freshwater layer at the free surface has a two-fold purpose. First it maintains an upper boundary condition of constant density. During each experiment, the vertical volume flux of freshwater into the experiment is free to adjust as required to reach a steady state. The advantage of using this method to maintain zero net volume flux is that it eliminates the question of where to place a physical sink in the experiment, which would constrain the density at its location to be at the mean density of the input sources when the flow is in equilibrium.

The second purpose of the freshwater layer is to set the surface stress. The freshwater flow rate is regulated by a needle valve in order to vary the magnitude of shear stress on the surface by adjusting the freshwater input volumetric flow rate. The resulting stress is directed from right to left so that it drives a flow in the same direction as that driven by the buoyancy forcing on the upper boundary.

3.3 Procedure & Measurements

The general procedure for each experiment spanned a total of three days. The saline water was mixed and allowed to equilibrate for at least 12 hrs prior to starting the experiment. The experiment tank was filled with fresh de-ionized water, and likewise allowed to sit overnight to degas and equilibrate. During the experiment, the tank was covered with insulation and allowed to run until statistical equilibrium. Conservatively, the time scale for equilibrium is given by the time required for the dense source plume to replace the fluid in the working volume, or $Q_d \mathscr{A}^{-1} = 7.36$ hrs, where $\mathscr{A}$ is the tank area. This "filling" timescale has been shown to provide a conservative upper limit on the time required to reach equilibrium (Stewart et al, 2012). All experiments were run for at least 6 filling timescales before the first set of data collection. The second set of data was collected 4 hrs subsequent to the completion of initial data collection. Equilibrium was reached when the overflow salinity asymptotically approached the mean salinity in the system, and the density profile obtained by the conductivity probe remained unchanged between data sets. Approximately 12 hrs before data were recorded, seeding particles were mixed into the dense water tank. Typically, the concentration of seeding particles in the dense water was 4.4 g m^{-3}. Experience dictated that seeding only the dense water source was enough to create a homogeneous dispersion of seeding particles in the region of interest by the time PIV images were recorded.

Once each experiment had run for at least 6 filling timescales, the outflow flow rate and density were recorded. All discrete density samples were measured with an Anton Paar DMA5000 density meter, accurate to 0.005 kg m^{-3}, previously calibrated with an ultra pure water liquid density standard. Following the outflow measurements, a conductivity profile was recorded. In order to convert the voltage output of the conductivity profile into a density value, a third-order polynomial fit was obtained from two separate calibrations, taken before and after the conductivity probe traversed through the volume. This fit consistently yielded R^2 values of ≥ 0.99. The density values of the standards were chosen to span the full density range used in each experiment, allowing for interpolation of all possible densities. A pre- and post- calibration was carried out to ensure that there was no significant electrical drift during the 38 min profile measurement. Generally, both curves tended to overlay one another, and an average of the two curves was used in calculating the final density profile.

After profiling was completed, synthetic schlieren images were recorded for 300 frames at 1 Hz and processed using a pattern matching algorithm developed by Dalziel Research

Table 1: Summary of experiments and relevant quantities. The velocity u_f refers to the flow rate of the freshwater layer, and is calculated by normalizing Q_f with the thickness of the freshwater layer it produces before any density anomalies are introduced into the working volume. $\Delta\rho_{max}$ is the maximum density difference between the source and sink. $\delta_{0.95}$ is the thickness of the boundary layer responsible for containing 95% of the maximum density difference in the working domain. ψ_{max} is the maximum streamfunction estimated from PIV measurements. Horizontal lines indicate experiments with poor PIV quality for which a measure of ψ_{max} could not be achieved.

Exp	u_f (mm s^{-1})	$\Delta\rho_{max}$ (kg m^{-3})	Ra_B	$S_{\delta f}$	$\delta_{0.95}$ (mm)	ψ_{max} (mm^{2}s^{-1})
1	2.2	33.24	3.13×10^{18}	0.121	2.03	247
2	2.3	13.17	1.17×10^{18}	0.162	1.52	80
3	3.5	23.42	2.16×10^{18}	0.168	3.56	–
4	6.8	32.87	3.10×10^{18}	0.285	3.45	214
5	5.5	23.03	2.12×10^{18}	0.337	5.18	–
6	5.1	13.16	1.16×10^{18}	0.400	3.45	89
7	8.8	33.07	3.13×10^{18}	0.416	40.23	898
8	10.4	22.76	2.10×10^{18}	0.579	145.29	1241
9	12.1	32.81	3.10×10^{18}	0.600	69.20	1499
10	10.1	13.19	1.17×10^{18}	0.731	76.50	–
11	13.5	22.87	2.11×10^{18}	0.878	205.13	1544
12	17.9	23.55	2.18×10^{18}	1.01	173.33	2025
13	14.6	13.02	1.15×10^{18}	1.19	150.67	2003
14	17.8	12.81	1.13×10^{18}	1.27	167.74	2165
15	19.5	32.60	3.10×10^{18}	1.28	103.73	2377

Partners, 2008 with a 15×15 px interrogation window, providing a final resolution of 12.5×12.5 mm. In addition, 200 PIV images were recorded at 10 Hz for 20 s. Considering the average velocities in the flow, this frequency was sufficient to resolve the bulk motion. All PIV results presented in this paper are temporally averaged over the 20 s acquisition period to adequately capture the eddying structures in the flow. The PIV sequences are pre-processed using standard techniques in order to facilitate calculation of the velocity fields. First, the image brightness and contrast are adjusted based on the intensity histogram of a region of interest (ROI). A 3×3 px median filter is applied to the resulting stack of images in order to reduce shot noise. The filtered image series is then subtracted from the original image series in order to correct for any background intensity variations. Finally, the image histogram is equalized to account for any overly bright spots that may bias processing. The resulting PIV images are processed using PIVlab (Thielicke, 2014). Before any calculations are carried out, a ROI is specified, followed by masking of stationary objects that protrude into the ROI, such as near the plume and freshwater sources. FFT window deformation was implemented as the cross-correlation algorithm, which analyzed the data in three passes, using a sequentially decreasing interrogation window area and 50% overlap. The final window size was 32×32 px, providing a final resolution of 12.2×12.2 mm. Between passes, missing velocity information was interpolated with a spline fit; this was not done after the final pass. Sub-pixel precision was achieved by fitting the intensity distribution of the correlation matrix with a 2D Gaussian function (Thielicke, 2014). Finally, spurious vectors were removed by setting upper and lower limits on the velocities, employing a standard deviation filter that rejects vectors outside of 3 standard deviations of the mean, and performing a

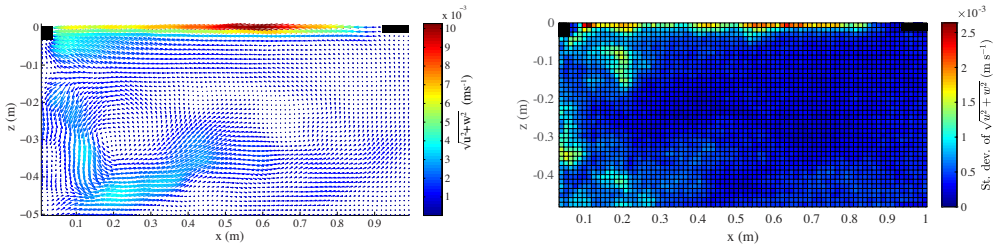

(a) (b)

Fig. 2: *(a)* Steady-state mean velocity field for an experiment with $S_{\delta f} = 0.12$. The colormap represents the velocity magnitude, which is a maximum near the tank surface where the stress is applied. *(b)* plots the standard deviation of the velocity magnitude. The black rectangles near the surface correspond to masked no-flow regions.

normalized median test with a threshold of 3 and $\varepsilon = 0.15$ (Westerweel and Scarano, 2005). The resulting velocity fields were smoothed before calculation of derivatives.

Dye images were recorded after the second set of data collection was completed at 0.2 Hz for approximately 25-30 minutes in order to visualize the steady-state circulation. A total of 15 experiments were carried out, spanning a freshwater volumetric flow rate of 19.4-165.6 mm^2s^{-1}. Table 1 summarizes the experiments and relevant quantities.

4 Results

4.1 Qualitative features

For small values of $S_{\delta f}$, the steady-state circulation exhibits similar qualitative flow features to those observed in prior work where the flow was driven by differential heating (e.g. Mullarney et al, 2004) as well as by a solutal buoyancy forcing (Stewart et al, 2012). Specifically, a turbulent plume descends the full depth of the tank along the left-hand wall, detraining into the interior along the bottom boundary. Upstream, the plume is narrow in that it does not occupy more than 20% of the tank length. The eddying outflow is distributed along the whole length of the tank base, and the circulation is closed via broad upwelling throughout the interior to the surface, with marked entrainment into the plume at all heights. Figure 2a plots a typical mean velocity field averaged over 20 seconds of steady-state flow for low values of $S_{\delta f}$, showing the eddying plume outflow into the tank interior, widespread upwelling, and global asymmetry of the circulation. Figure 2b plots the standard deviation of the velocity magnitude, revealing a steady interior flow with peak deviations in regions of turbulence, such as in the plume outflow, and along the surface corresponding to the freshwater flow.

For experiments where $S_{\delta f} > 0.42$, the stratification near the freshwater inlet is no longer able to effectively dampen shear-induced perturbations, resulting in a region of localized mixing. This region of mixing is clearly visible in dye images as well as PIV data, and drastically alters the flow field. Once mixing develops, the water entrained by the plume near the surface freshens, creating a local negative buoyancy deficit and causing the plume to detrain at partial depth. All experiments that exhibited a partial-depth circulation also featured a laminar sublayer that developed against the left-hand wall. The sublayer allowed

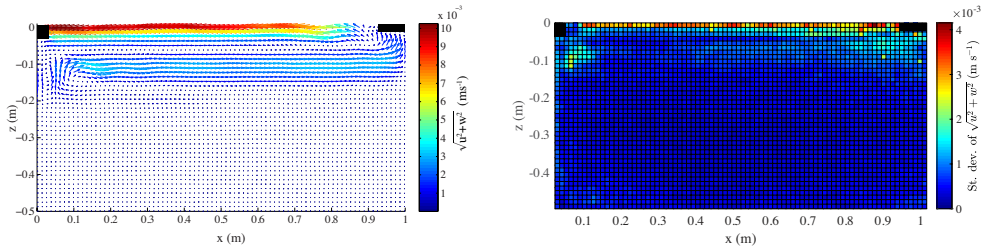

(a) (b)

Fig. 3: *(a)* Steady-state mean velocity field for an experiment with $S_{\delta f}$ = 0.88. The colormap represents the velocity magnitude, which is a maximum near the tank surface where the stress is applied. *(b)* plots the standard deviation of the velocity magnitude. The black rectangles near the surface correspond to masked no-flow regions.

plume outflow to reach the base of the tank, creating a layer of relatively dense water at the base. Figure 3a plots a typical mean velocity field averaged over 20 seconds of flow for experiments with $S_{\delta f} > 0.42$, displaying a plume that detrains into the interior at an intermediate depth. In contrast to the observed circulation for $S_{\delta f} < 0.42$, the flow field exhibits a larger degree of symmetry. The interior vertical velocity of the plume outflow is confined to a region of upwelling near the boundary opposite the one at which the plume is forced, as opposed to the broadly distributed interior upwelling characteristic of experiments in which $S_{\delta f} < 0.42$. Figure 3b plots the corresponding standard deviation of the velocity magnitude, illustrating the relatively steady nature of the flow excepting at the surface, where the freshwater layer introduces some unsteadiness to the flow.

4.2 Quantitative features

Figure 4a plots the normalized buoyancy measured at the maximum extent of the conductivity probe's reach, $b(-H/2)$, as a function of $S_{\delta f}$. The normalized buoyancy decreases monotonically with increasing stress for fixed Ra_B, indicating that the environment is becoming fresher with increasing stress. Moreover, the interior normalized buoyancy decreases with increasing Ra_B, at fixed $S_{\delta f}$.

Profiles of the horizontally-averaged interior upwelling velocity outside of the plume region, W_e, are shown in Figure 4b for select experiments. The profile shapes are qualitatively similar to those reported in Hughes et al (2007), obtained from numerical simulations by Mullarney et al (2004). For experiments with $S_{\delta f} < 0.42$, the average interior velocity profile is nonzero for the full extent of the domain. For experiments with $S_{\delta f} > 0.42$, the velocity profiles tend toward 0 mm s^{-1} at varying depths, revealing relatively stagnant regions below corresponding detrainment levels. All profiles support the general trend of increasing W_e with depth due to entrainment into the plume.

Qualitative and quantitative data both reveal a laminar sublayer against the endwall adjacent to the plume when $S_{\delta f} > 0.42$. Relatively dense fluid along the bottom boundary is evident in profiles of the buoyancy frequency, defined as $N^2 = -g\rho_0^{-1}(\partial\rho/\partial z)$. These profiles were obtained from synthetic schlieren measurements by averaging the vertical density gradient outside of the plume and mixing regions. Figure 5a displays N^2 normalized by the maximum buoyancy. The buoyancy frequency at the bottom boundary is invariably stable

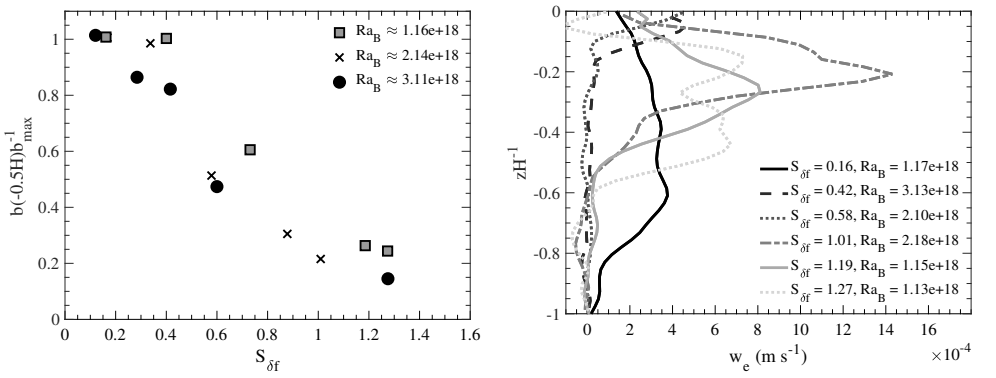

Fig. 4: Panel *(a)* plots the normalized buoyancy in the interior at the conductivity probe's maximum penetration depth, approximately $-0.5H$, as a function of $S_{\delta f}$. Each symbol corresponds to a different value of Ra_B as indicated in the legend. Panel *(b)* plots the mean profiles of the interior vertical velocity, W_e, obtained from PIV measurements. The mean vertical velocity corresponds to the horizontally averaged W_e outside of the plume.

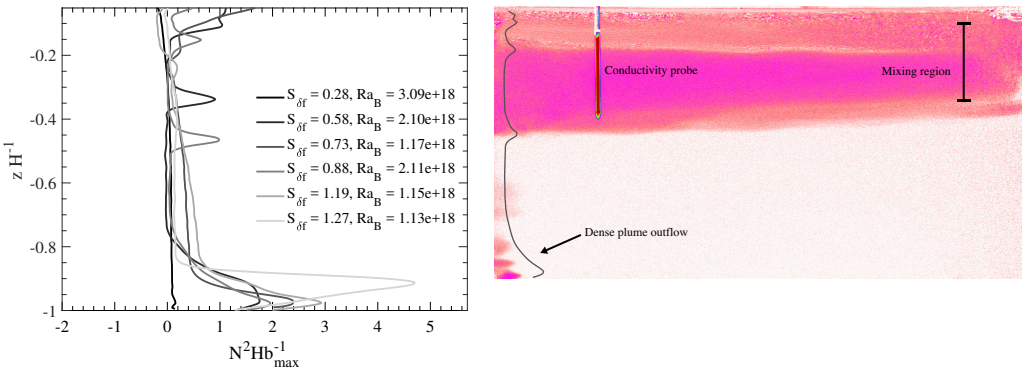

Fig. 5: Panel *(a)* displays profiles of normalized buoyancy frequency obtained from synthetic schlieren measurements for various values of $S_{\delta f}$. The stratification profile indicates that a laminar sublayer feeds dense fluid to the bottom of the tank. Panel *(b)* is a snapshot of the steady-state plume outflow with its corresponding N^2 profile superposed on the dye image for an experiment with $S_{\delta f} = 0.88$. The profile correlates well with the location of density gradients. The laminar sublayer is evident at the bottom boundary.

and increases with $S_{\delta f}$, in agreement with freshening interior waters as $S_{\delta f}$ is increased. Figure 5b is a snapshot of the steady-state plume outflow with the corresponding N^2 profile superposed on its dye image. Undulations in the N^2 profile correlate well with pronounced regions of strong density gradient; small finger-like intrusions of dyed fluid expose the laminar sublayer at the tank bottom against the endwall. Discrete density measurements of fluid from the bottom left-hand corner of the tank confirm that the average density within the

sublayer is approximately 99% of the maximum density anomaly. The implications of the laminar sublayer are further discussed in Sec. 8.

5 Stability and adjustment

The surface shear imposed by the layer of freshwater excites instabilities if it can overcome the suppressing effects of the vertical stratification beneath it. Some insight into the threshold for instability may be obtained by considering the gradient Richardson number between the freshwater layer and underlying circulation,

$$Ri = \frac{N^2}{(\partial u/\partial z)^2}. \tag{10}$$

For continuously stratified parallel flows, the system is susceptible to Kelvin-Helmholtz-type instabilities if there exists a critical value of Ri somewhere in the flow such that $Ri_c = Ri < 0.25$. Alternatively, a turbulent flow is expected to become stable when $Ri_T = Ri > 1$ (Stull, 1988). While this does not always apply to all distributions of $u(z)$ and $N(z)$, these threshold values remain a useful measure by which to predict instability of a stratified shear layer (Kundu et al, 2012). In the present experiments, the region near the freshwater source is unstable from the onset of the experiment, and only becomes stable once a vertical stratification develops that is strong enough to inhibit growing modes. Thus, the sought-after value of Ri is expected to be closer to Ri_T. Although profiles of $N^2(z)$ are readily available from conductivity probe measurements, the vertical gradient of the horizontal velocity near the interface of the freshwater layer and underlying circulation is too sharp to be resolved by the current PIV system. Therefore, a parameterization of Ri, or the bulk Richardson number, Ri_B, is used instead, defined as

$$Ri_B = \frac{g\Delta\rho\Delta z}{\rho_0 U_{max}^2}, \tag{11}$$

where $\Delta\rho$ is the density difference between the upper and lower layer over the thickness Δz, and the lower layer is assumed to be stationary relative to the fast-moving freshwater layer so that the vertical gradient of the horizontal velocity is parameterized by $\partial u/\partial z \sim \Delta u \Delta z^{-1} \sim U_{max}\Delta z^{-1}$. Critical values of Ri_B are expected to approach Ri_c and Ri_T in the limit $\Delta z \to 0$. Figure 6 shows a log-log plot Ri_B as a function of $S_{\delta f}$, using values obtained during the experiment (i.e. not *a priori*). The black squares correspond to experiments with no apparent mixing, and white circles mark experiments in which mixing was present, as indicated by the presence of an eddy in the upper right-hand corner of the experiment tank and a partial-depth plume. The log-log plot reveals a transition in slope near $S_{\delta f}$ = 0.42, suggesting a new flow regime. The experiment closest to the threshold value of $S_{\delta f} = 0.42$ corresponds to $Ri_B = 1.25$; experiments with $S_{\delta f}$ values beyond this point maintain $Ri_B < 0.22$. Figure 6 corroborates the notion that for experiments in which $S_{\delta f} > 0.42$, the developed stratification will no longer be able to dampen perturbations caused by the surface shear, and will thus form a region of localized turbulence.

The input of mechanical energy by the surface stress creates turbulent motion which works to transport buoyancy downward a finite distance, consequently thickening the boundary layer. On the other hand, the imposed buoyancy flux is working to reduce the boundary layer thickness. Thus, a steady-state depth, d_{eq}, is expected to exist where the two forces balance. Noting that the depth of mixing is approximately linearly proportional to $S_{\delta f}$ in the

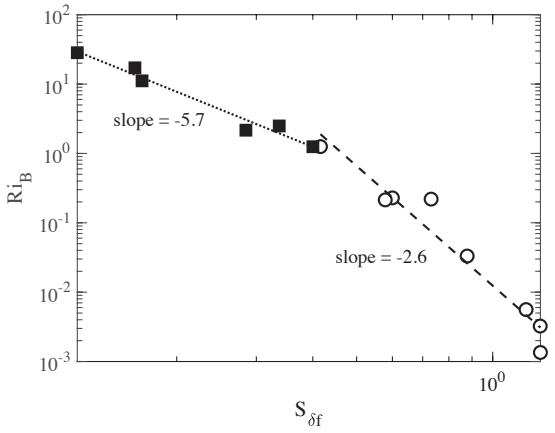

Fig. 6: Ri_B as defined in eqn. (11) plotted as a function of $S_{\delta f}$ on a log-log plot with corresponding fitted lines. Black squares and white circles denote experiments without and with mixing, respectively. The experiment closest to the threshold value of $S_{\delta f} = 0.42$ corresponds to $Ri_B = 1.25$; experiments with $S_{\delta f}$ values beyond this point maintain $Ri_B < 0.22$.

range considered, dimensional analysis dictates that

$$d_{eq} = a\frac{U_{max}\nu^{1/2}L^{1/2}}{B_0^{1/2}}, \tag{12}$$

where a is a constant, found to be approximately equal to 20, and B_0 is the specific buoyancy flux, equal to,

$$B_0 = g\beta S_d Q_d, \tag{13}$$

where β is the coefficient of expansion for salt, equal to 0.69 (Sharqawy et al, 2010), and S_d is the dense water salinity. Figure 7 plots the measured and scaled mixing depths. The mixing depth scaling in eqn. (12) is also compared to two other scalings in literature that are relevant to flows where both buoyancy and mechanical forcing are imposed on a flow, namely the Monin-Obukhov length, d_{mo}, and its modified version, d_{hl}, that takes into consideration the decay of turbulent kinetic energy with distance from the source for the case of zero-mean-shear turbulence superposed on a stabilizing buoyancy flux (Hopfinger and Linden, 1982),

$$d_{mo} = a_{mo}\frac{u_*^3 L}{B_0}, \qquad d_{hl} = \left[\frac{u_*^3 L}{B_0}\right]^{1/4}, \tag{14}$$

where a_{mo} is a constant equal to approximately 200, and u_* is the friction velocity. The latter scaling agrees more closely with experiment measurements compared to d_{mo}, and may be more relevant for the system under consideration as turbulent motions are expected to decay away from the mixing source, which is the case here. When d_{hl} is recast in terms of U_{max},

$$d_{hl} = \frac{\nu^{3/8}U_{max}^{3/8}L^{1/4}}{\delta_f^{3/4}B_0^{1/4}} \sim \frac{\nu^{3/8}U_{max}^{3/8}}{B_0^{1/4}}, \tag{15}$$

the scaling is a relatively weaker function of B_0 in comparison to d_{eq}. Both scalings adequately model the mixing depth as a function of $S_{\delta f}$ for the experiment range considered, with d_{eq} offering slightly better agreement, specifically for smaller $S_{\delta f}$.

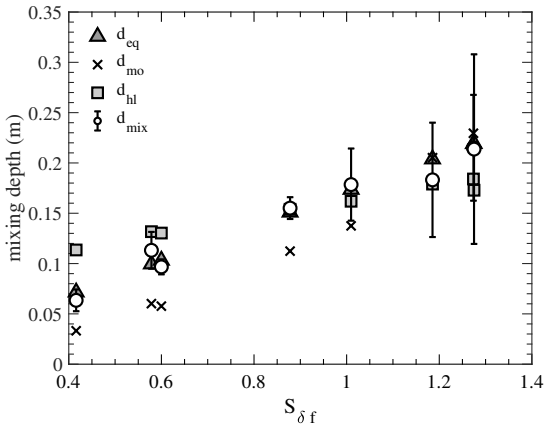

Fig. 7: Scaling of the equilibrium mixed layer depth, d_{eq}, derived from the approximately linear relationship between the mixing depth, d_{mix}, and $S_{\delta f}$. Scalings are plotted along with the Monin-Obukhov length scale, d_{mo}, and a modified length scale by Hopfinger and Linden (1982), d_{hl}, for reference.

6 Filling box model

An idealized schematic of the experiment setup presented in Sect. 3 is considered in the following analysis. The vertical coordinate z is taken to be 0 at the plume origin and increasing upwards. The ejection of fluid from the interior is idealized to occur uniformly over the length of the tank as the whole surface boundary is free to respond to the mechanism of diffusion. For small aspect ratios and in the case of no mechanical forcing, the flow outside of the plume is generally uniform in the horizontal where it is characterized by a slow upwelling toward the surface. When mixing is present, the flow is likewise uniform outside of the plume and the mixing region. In reality, given the aspect ratio in the present study, the plume outflow does introduce some 2D structure to the velocity field (cf. Figure 2a). However, in order to make analytical progress, we approximate the system with a one-dimensional model in which the plume outflow is assumed to be instantaneously distributed in the horizontal (Manins, 1979; Hughes et al, 2007). The model presented in this paper follows the equations describing a 2D line half-plume discussed in detail in Hughes et al (2007). The authors derive a recycling box model for horizontal convection by adjusting the filling-box flow equations of Baines and Turner (1969) to take into consideration an advection-diffusion balance of the density field in the interior of the domain. For brevity, only the nondimensionalized equations will be presented, and the reader is referred to Hughes et al (2007) for the full derivation of the requisite equations. The dimensionless variables ζ, r, b_p, b_e, w_p, and w_e represent the vertical coordinate, the plume thickness, the specific buoyancy on the plume axis, the interior specific buoyancy, the vertical velocity of the plume, and the interior vertical velocity, respectively. Nondimensionalizing the continuity, momentum, and buoyancy equations,

$$\frac{\mathrm{d}}{\mathrm{d}\zeta}(rw_p) = w_p, \tag{16}$$

$$\frac{\mathrm{d}}{\mathrm{d}\zeta}(rw_p^2) = rb_p, \tag{17}$$

$$\frac{\mathrm{d}}{\mathrm{d}\zeta}(rw_p b_p) = rw_p \frac{\mathrm{d}b_e}{\mathrm{d}\zeta}. \tag{18}$$

The vertical coordinate ζ is taken to be 0 at the plume origin and decreasing in the direction of flow in the plume. The chosen coordinate system dictates that the plume centerline velocity, w_p, will be negative. Additionally, the plume centerline buoyancy, b_p, will always be negative since the plume is sinking and therefore maintains a negative buoyancy by convention. The nondimensional equation for the conservation of volume in the interior is,

$$rw_p = -w_e, \tag{19}$$

and for the advection-diffusion balance in the interior,

$$w_e \frac{\mathrm{d}b_e}{\mathrm{d}\zeta} = \frac{\mathrm{d}}{\mathrm{d}\zeta}\left[\gamma(\zeta)\frac{\mathrm{d}b_e}{\mathrm{d}\zeta}\right], \tag{20}$$

where

$$\gamma = \frac{\kappa^*\big|_\zeta}{\kappa^*\big|_{\zeta=0}}. \tag{21}$$

The parameter γ encompasses a spatially varying turbulent diffusivity, which is necessary to describe correctly the localized region of mixing generated by the surface stress. The boundary conditions at $\zeta = 0$ are of zero volume and momentum, and that the specific buoyancy flux must be equal to the diffusion of buoyancy out of the domain at the same level, ensuring that there is zero net input of buoyancy into the system. The dimensionless specific buoyancy flux in the plume is defined as $\phi(\zeta) = rw_p b_p$, so that the boundary condition for buoyancy is,

$$\phi(0) = \gamma(0)\left[-\frac{\mathrm{d}b_e(0)}{\mathrm{d}\zeta}\right] = 1, \tag{22}$$

noting that b_e is always positive. In order to arrive at a fourth-order system, eqn. (19) is substituted into eqn. (20), equated with conservation of buoyancy in eqn. (18), and integrated from $\zeta' = 0$ to $\zeta' = \zeta$. Applying the boundary condition given in eqn. (22), the result is,

$$\frac{\mathrm{d}b_e}{\mathrm{d}\zeta} = \frac{-\phi(\zeta)}{\gamma}. \tag{23}$$

Defining $Q = rw_p$, the other three equations describing the system are,

$$\frac{\mathrm{d}\phi}{\mathrm{d}\zeta} = Q\frac{\mathrm{d}b_e}{\mathrm{d}\zeta}, \tag{24}$$

$$\frac{\mathrm{d}Q}{\mathrm{d}\zeta} = \frac{Q^2}{r}\frac{1}{Q}, \tag{25}$$

and

$$\frac{\mathrm{d}}{\mathrm{d}\zeta}(Q^2/r) = \phi Q\frac{r}{Q^2}, \tag{26}$$

subject to the boundary conditions $\phi(0) = 1$, $Q(0) = 0$, $Q^2/r(0) = 0$, and $b_e(0) = 0$. In practice, the line half-plume has a finite input of mass equal to Q_d through the stainless steel tubing. Any initial momentum is assumed to be dissipated before entering the working volume. The input is assumed to be that of a pure plume driven solely by a buoyancy flux. A virtual source correction is applied to the solutions in order to correct for the finite mass flux (Stewart et al, 2012).

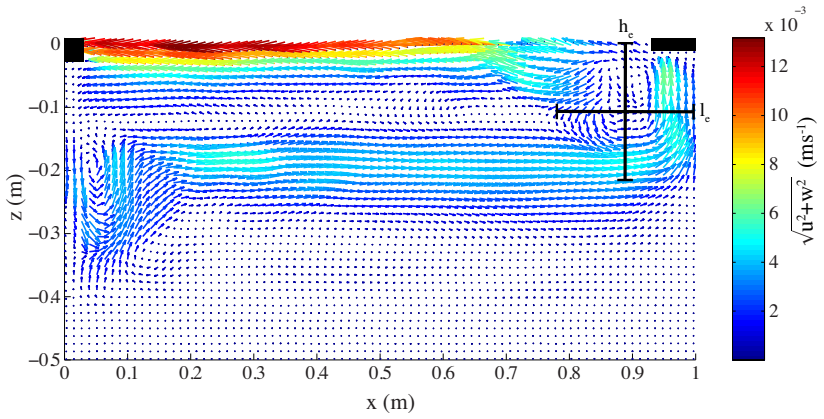

Fig. 8: Velocity field for an experiment where $S_{\delta f} = 1.25$, obtained from PIV measurements. The horizontal and vertical extents of the eddy, l_e and h_e, respectively, are depicted by corresponding arrows. The two black rectangles at the surface correspond to masked no-flow regions.

6.1 Estimation of the turbulent diffusivity

In order to estimate the magnitude of the turbulent mixing coefficient in the region of mixing, κ^* is parameterized by the characteristics of the developed eddy via the relation (Pope, 2000),

$$\kappa^* \propto u^* h_e \quad \mathrm{m^2 s^{-1}}, \tag{27}$$

where h_e is the vertical diameter of the eddy, and u^* is its rms velocity, defined as,

$$u^* = \sqrt{\mathrm{rms}(u'^2) + \mathrm{rms}(w'^2)}. \tag{28}$$

Here, u' and w' are deviations from the mean velocity field, with $u' = u - \overline{u}$ and $w' = w - \overline{w}$. An example of such an eddy is shown in Figure 8 for an experiment with $S_{\delta f} = 1.25$. The eddy length and height are determined from PIV data by locating where the vertical and horizontal velocity gradient reached a maximum in a line plot through the eddy, respectively, thus indicating its perimeter. The fitted relation between $S_{\delta f}$ and κ^* is found to be

$$\kappa^* = c(5.07 \times 10^{-4} S_{\delta f}^{2.6}) \quad \mathrm{m^2 s^{-1}}. \tag{29}$$

To solve for the constant of proportionality, c, an empirical estimate of κ^* is also obtained by considering the inverse problem, and fitting measured buoyancy profiles to that calculated from the solution of the recycling box equations. Comparing this value to the eddy-derived κ^*, the two diffusivities differ by a mean constant value of $c = 0.0287$. Thus, the final functional form of κ^* is

$$\kappa^* = 1.45 \times 10^{-5} S_{\delta f}^{2.6} \quad \mathrm{m^2 s^{-1}}. \tag{30}$$

A piecewise profile is used for $\kappa(\zeta)$, in which κ^* takes on a fitted value given by eqn. (30) from the surface $\zeta = 0$ until the normalized depth of mixing, $\zeta_d = d_{mix} H^{-1}$, beneath which $\kappa^* = \kappa_{mol}$, taken to be 1.38×10^{-9} $\mathrm{m^2 s^{-1}}$ (Benítez, 2009). For experiments with no apparent mixing, the value of κ^* is 2.67×10^{-9} $\mathrm{m^2 s^{-1}}$, as estimated by Stewart et al (2012) in the case of buoyancy-driven convection experiments with no external mechanical forcing. The final profile for $\gamma(\zeta)$ for each experiment is obtained by normalizing $\kappa^*(\zeta)$ by $\kappa^*(0)$.

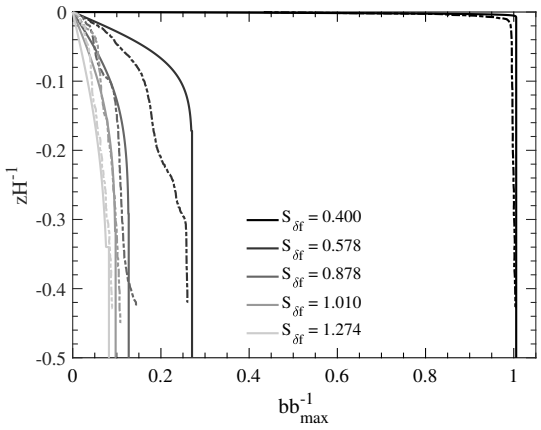

Fig. 9: Normalized buoyancy profiles for select values of $S_{\delta f}$. Dashed lines indicate conductivity probe measurements and solid lines are the solutions to the plume equations.

6.2 Results of the modified recycling box model

Figure 9 displays normalized buoyancy profiles obtained from conductivity probe measurements (dashed lines) as well as corresponding solutions to the recycling box model (solid lines) for various values of $S_{\delta f}$.

In order to compare correctly the experiment density profiles to those obtained by solving the system of equations given in (23)-(26), the first few data points in the conductivity profile which correspond to the surface freshwater layer are discarded. For experiments with $S_{\delta f} > 0.42$, the minimum density in the tank is then taken to be the interfacial density, since regional mixing near the freshwater source ensures that there is no freshwater in the working volume. The density steps visible in a few of the measured profiles correspond to the point at which the probe passes through the outflow of the mixing region; this is most apparent in the dye visualization in Figure 5b. While the mixing region occurs over a large depth, the outflow is much shallower and at a fresher density than the inflow. The result is a discontinuity in the density profile, which is evident in the theoretical profiles only when the mixing depth is equal to the depth of inflow into the plume, typically for flows with large $S_{\delta f}$.

Generally, as $S_{\delta f}$ is increased, the fluid density in the environment becomes fresher at all measured depths. Also evident from Figure 9 is the gradual thickening of the boundary layer for increasing $S_{\delta f}$, as the upper layer is homogenized by the localized turbulence. The approximate profile shape is generally recovered by the solutions to the plume equations.

The dimensionless solutions to key quantities, including the maximum density difference, $\Delta b_e(\zeta_h)$, the thickness of the boundary layer that incorporates 95% of the density anomaly, $\delta_{0.95}$, and the corresponding interior vertical velocity at the boundary layer, $w_e(\delta_{0.95})$, are shown in Table 2, where $\zeta_h = \delta_{bl}^{-1} h$ is the effective dimensionless box depth.

All values for experiments with $S_{\delta f} < 0.42$ match exactly those predicted by the recycling box model of Hughes et al (2007), valid in the limit $\phi \to 0$. The asymptotic approximations vary at most 0.01% from the mean value. For the explored range of values when $S_{\delta f} > 0.42$, the solutions for $\Delta b_e(\zeta_h)$ and $\delta_{0.95}$ vary within 0.85% and 7.5% of the mean, respectively.

Table 2: A summary of the asymptotic solutions to plume equations. For $S_{\delta f} < 0.42$, the quantities match exactly those predicted by the recycling box model of Hughes et al (2007). For $S_{\delta f} > 0.42$, the solutions become functions of $S_{\delta f}$; the mean and standard deviation for each quantity are presented.

	$S_{\delta f} < 0.42$	$S_{\delta f} > 0.42$
$\Delta b_e(\zeta_h) =$	1.28	1.29 ± 0.011
$\delta_{0.95} =$	2.06	2.00 ± 0.15
$w_e(\delta_{0.95}) =$	1.83	1.79 ± 0.114

For a clearer comparison with experiment results, the solutions to the streamfunction, maximum density difference, and boundary layer thickness are recast into dimensional quantities (Hughes et al, 2007):

$$\psi_{max} = 2E^{1/2}\left(\frac{H}{L}\right)^{1/2} B_{vs}^{1/4} L^{3/4} \kappa^{*1/4}, \tag{31}$$

$$\left.\frac{\rho_e - \rho_0}{\rho_0}\right|_{max} = C_{\Delta b_e} \times 2^{-1/6} E^{-1/3} g^{-1} L^{-1/2} B_{vs}^{5/6} \kappa^{*-1/2}, \tag{32}$$

$$\delta_{0.95} = C_{\delta_{0.95}} \times 2^{-1/6} E^{-1/3} B_{vs}^{-1/6} L^{1/2} \kappa^{*1/2}, \tag{33}$$

where $C_{\Delta b_e}$ and $C_{\delta_{0.95}}$ are the solutions predicted by the theoretical model, and B_{vs} is the specific buoyancy flux at the virtual source. Experimental measurements (circles) along with theoretical fits (squares) are displayed in Figure 10.

Error bars in the calculations of the streamfunction and density arise from averaging two recorded data sets per each experiment, at half a filling timescale apart. For experiments with $S_{\delta f} < 0.42$, errors in the density measurement are relatively low. However, once localized mixing occurs, and specifically for experiments near the transition into mixing, the conductivity profiles are noisier, evident by the magnitude of the error bars in Figure 10b. The eddying nature of the flow field is likely causing $O(1)$ s fluctuations which are picked up in the conductivity profile. At the limit of the conductivity probe's traverse, the flow was more stable. Given that the errors are largest near the transition point of $S_{\delta f} = 0.42$, the flow may be adjusting, specifically within the boundary layer, to the regime in which the stratification can no longer suppress perturbations induced by the surface shear.

7 Discussion

At the onset of each experiment, the plume is entering a homogeneous, freshwater environment, in which it necessarily maintains sufficient specific buoyancy and momentum to sink the full depth of the volume. Qualitative observations of the equilibration process verify that the plume penetrates the full depth of the volume on its initial descent. Because the plume exists in a confined space, its outflow inevitably interacts with the region of developed turbulence near the freshwater source. If stabilizing mechanisms such as viscosity and stratification become too weak to suppress instabilities near the surface, turbulent motions will mix the surrounding fluid. The result is a mixed layer that increases in depth as the flow evolves, ultimately extending to d_{mix}, an equilibrium depth. During this transient adjustment, the plume is continually subject to an input of stabilizing buoyancy in the form of

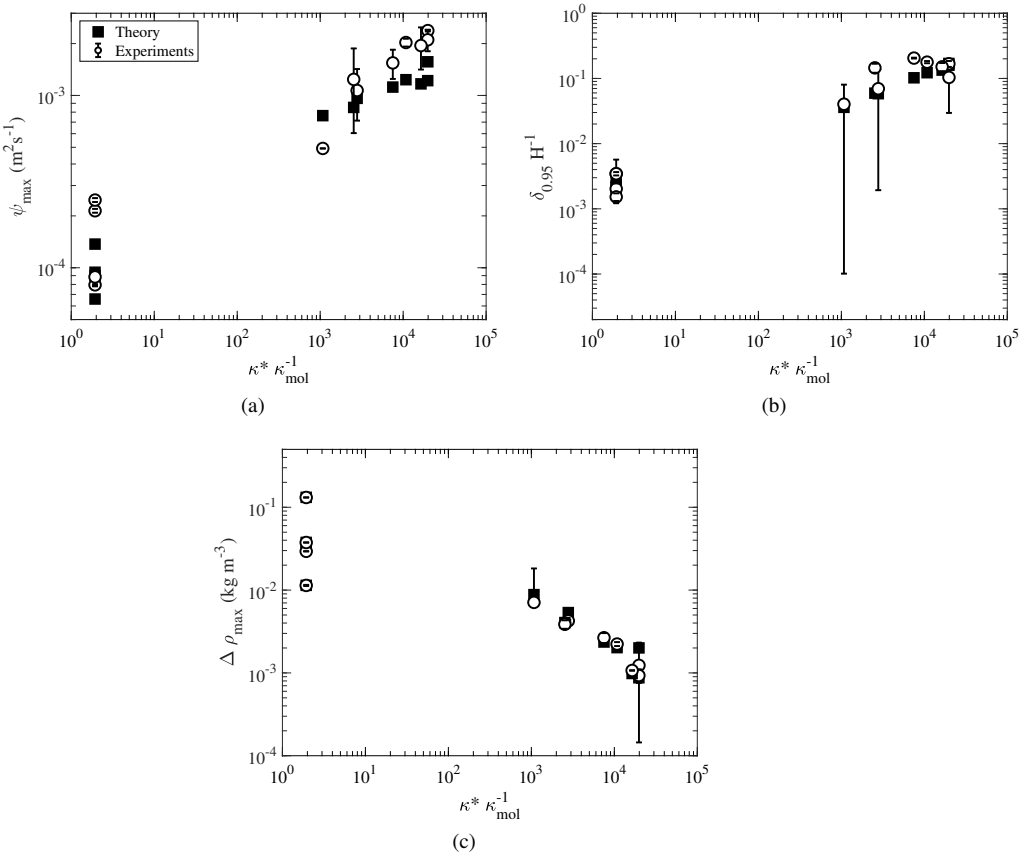

Fig. 10: Summary of key experimental quantities (circles) as well as recycling box model predictions (squares). All error bars are estimated from averaging two data sets per experiment, taken approximately 4 hrs apart. Panel *(a)*, *(b)* and *(c)* plot the streamfunction, normalized boundary layer thickness, and maximum density difference as a function of $\kappa^* \kappa_{mol}^{-1}$, respectively.

fresher fluid, resulting in a weakened plume that loses its momentum flux before it is able to penetrate the full domain. Consequently, the plume finds itself in a stratified environment which, below a certain level, is denser than it, causing it to detrain at variable depth into the tank interior.

Figure 10 suggests that the experimentally-measured quantities of the boundary layer thickness and maximum streamfunction are larger than predicted by the solutions to the equations. A thicker boundary layer is consistent with a larger streamfunction, since a larger volume of water will be entrained by the plume before it is exhausted of its buoyancy forcing. The increase in boundary layer thickness may be caused by inhibited upwelling due to the surface stress. While the flow may be in a slowly evolving quasi-steady state, the maximum density difference is predicted within measurement uncertainty. This lends support to the notion that the plume is in fact the primary transporter of density anomalies within the

volume and sets the bulk of the flow field, with molecular diffusion playing a minor role in adjusting the final density gradient.

The formation of a laminar sublayer on the wall adjacent to the plume outflow permits dense water to penetrate past the plume detrainment depth, and eject dense fluid into the stagnant waters. It is possible that the input of fresher waters from localized mixing drops the local Ra_B value into a transitional region between laminar and turbulent flow, thus supporting sublayer formation. Because it resupplies dense fluid into the stagnant region of the flow, diffusion cannot erode away the interface between the plume and quiescent layer. Maintenance of a steady-state partial-depth circulation could then be achieved if the advection of buoyancy flux by the laminar sublayer is exactly matched by diffusion across the interface separating the circulation and underlying stagnant region, such that the horizontally-averaged net buoyancy flux at any given depth is zero. If the plume were not against an endwall, there would be no support for the laminar sublayer, and the partial-depth circulation would only be a transient response to the increase in stabilizing buoyancy, with a full-depth penetration being the final flow configuration. The existence of the endwall and its support of a laminar sublayer then limits the results of this particular study to plumes that develop immediately adjacent to a boundary.

8 Conclusions

A series of experiments have been performed in which a surface buoyancy-forced circulation, driven by salt fluxes, is subject to a surface stress in the form of a freshwater layer flowing along the same boundary at which the convection is forced. When the ratio of mechanical to buoyancy forcing, $S_{\delta f}$, exceeds 0.42, a region of mixing persists near the freshwater inlet, which thereafter deepens approximately linearly with increasing $S_{\delta f}$. The resulting turbulent mixing coefficient, $\kappa^*(z)$, is no longer uniform in the vertical, and must be parameterized by the characteristics of the developed eddy in the turbulent region. The value of $\kappa^*(z)$ is found to approximately scale with $S_{\delta f}^{2.6}$. The depth of the mixing region develops until it reaches an equilibrium level, which is estimated well by the corresponding ratio of mechanical to buoyancy forcing. During its spatial development, the mixing region imparts a temporal input of stabilizing buoyancy into the plume, causing it to weaken and consequently detrain into the interior at partial depth. Furthermore, a laminar sublayer develops on the left-hand endwall adjacent to the plume outflow, supplying dense plume fluid into the relatively quiescent interior. Generally, the partially-sinking plume does not exhibit signs of penetrative convection at the interface of the plume outflow and underlying stagnant region, which would otherwise reduce the timescale required to obtain equilibrium. As a result, it is unclear if the partial-depth circulations are equilibrated flows. Due to the existence of a laminar sublayer, it is possible to maintain zero net buoyancy flux through any level in the fluid, and therefore the system may have in fact reached a well-defined steady-state. With the available data, there is no way of exploring this speculation. Additional experiments, specifically ones in which the convection is driven by a thermal forcing, are required, as they can be run for the long diffusive timescale, ensuring that a steady-state is reached. The mechanism of penetrative convection also requires further investigation in order to determine under what conditions horizontal convection will reestablish itself on the timescale observed in Vreugdenhil et al (2016) following a net input of buoyancy flux into the plume.

The solutions of the recycling box model equations with nonuniform $\gamma(\zeta)$ agree well with key flow characteristics, supporting the main result that the $O(1)$ effect of a surface stress imposed in the same direction as the flow generated by surface buoyancy fluxes is

to impart mechanical energy into the circulation by creating a spatially-varying turbulent diffusivity. The model can be improved by using a more accurate function than one which is piecewise constant to describe the vertical profile of $\kappa^*(z)$. The solutions for the maximum streamfunction and boundary layer thickness are generally larger than their theoretical counterparts. A thicker boundary layer is consistent with an increase in the streamfunction, and boundary layer thicknesses approximately 20% greater than the corresponding theoretical prediction have been reported in experiments where mixing is confined to the upper portion of the domain using the same experimental setup as in the current study (Vreugdenhil et al, 2016). It is yet unclear why this is the case for confined mixing. In contrast, Stewart et al (2012) report thinner-than-predicted boundary layers for full-depth mixing.

The experimental results generally apply to the oceans and other large bodies of water subject to wind stress. If strong enough, the wind stress can induce regional turbulence extending from the surface to some intermediate depth. This small-scale turbulence will act to homogenize the layer in which it persists, consequently deepening the thermocline and altering the characteristics of the upper ocean. Additionally, near sinking regions, the mixed layer will modify the plume density through the entrainment of this relatively fresh fluid, resulting in a weakened plume that intrudes at partial depth. If the circulation is exposed to an oscillatory mechanical forcing for timescales on the order of the system's natural response timescale, any changes in magnitude and/or direction of the forcing can lead to changes in the bulk stratification, as the plume would once again alter its intrusion depth to accommodate the net supply of (de)stabilizing buoyancy. A series of such events can lead to complicated stratification profiles that extend beyond the depth of mixing induced by the surface stress, which is itself a function of the magnitude of the stress. The clearest example of this scenario is shown in Figure 5a, where the superposition of experiments subject to variable forcing can result in a global stratification profile that is much more complicated than one arising from a buoyancy-driven system. Additionally, near topographic boundaries, if a turbulent sinking plume is accompanied by a laminar sublayer, it can further modify the stratification profile by allowing dense fluid to reach deeper levels. The overarching result is that changes in the upper boundary layer can be communicated to the interior through advection by the plume, altering the global flow structure in response to a long-term perturbation.

Acknowledgements The authors would like to thank Dr. Eugene Pawlak for the use of his laser equipment, as well as Thomas Chalfant and Nicholas Busan for their assistance in building experiment components. We are also extremely grateful to Drs. Kial Stewart, Ross Griffiths, and James Rottman for thoughtful discussion and insight on the subject matter.

References

Baines WD, Turner JS (1969) Turbulent buoyant convection from a source in a confined region. J Fluid Mech 37:51–80

Beardsley RC, Festa JF (1972) A numerical model of convection driven by a surface stress and non-uniform horizontal heating. J Phys Oceanogr 2:444–455

Benítez J (2009) Principles and modern applications of mass transfer operations, 2nd edn. John Wiley & Sons

Chiu-Webster S, Hinch EJ, Lister JR (2008) Very viscous horizontal convection. J Fluid Mech 611:395–426

Dalziel Research Partners (2008) DigiFlow User Guide

Dewar WK, Bingham RJ, Iverson RL, Nowacek DP, St Laurent LC, Wiebe PH (2006) Does the marine biosphere mix the ocean? J Mar Res 64:541–561

Gayen B, Griffiths RW, Hughes GO, Saenz JA (2012) Energetics of horizontal convection. J Fluid Mech Rapids 716:R10–1–R10–11

Gayen B, Griffiths RW, Hughes GO (2014) Stability transitions and turbulence in horizontal convection. J Fluid Mech 751:698–724

Hazewinkel J, Paparella F, Young WR (2012) Stressed horizontal convection. J Fluid Mech 692:317–331

Hopfinger EJ, Linden PF (1982) Formation of thermoclines in zero-mean-shear turbulence subjected to a stabilizing buoyancy flux. J Fluid Mech 114:157–173

Hughes GO, Griffiths RW (2006) A simple convective model of the global overturning circulation, including effects of entrainment into sinking regions. Ocean Model 12:46–79

Hughes GO, Griffiths RW (2008) Horizontal convection. Annu Rev Fluid Mech 40:185–208

Hughes GO, Griffiths RW, Mullarney JC, Peterson WH (2007) A theoretical model for horizontal convection at high rayleigh number. J Fluid Mech 581:251–276

Ilicak M, Vallis GK (2012) Simulations and scaling of horizontal convection. Tellus A 64:18,377

Kanda I (2002) Conductivity Measurement System

Kuhlbrodt T, Griesel A, Montoya M, Levermann A, Hofmann M, Rahmstorf S (2007) On the driving processes of the atlantic meridional overturning circulation. Reviews of Geophysics 45:(RG2001)

Kundu PK, Cohen IM, Dowling DR (2012) Fluid Mechanics, 5th edn. Elsevier Inc.

Ledwell JR (2017) Comment on "Abyssal upwelling and downwelling driven by near-boundary mixing". Journal of Physical Oceanography 48:739–748

Linden PF (1999) The fluid mechanics of natural ventilation. Annu Rev Fluid Mech 31:201–238

Manins PC (1979) Turbulent buoyant convection from a source in a confined region. J Fluid Mech 91(4):765–781

McDougall TJ, Ferrari R (2018) Reply to "Comment on 'Abyssal upwelling and downwelling driven by near-boundary mixing"'. Journal of Physical Oceanography 48:749–753

Mullarney JC, Griffiths RW, Hughes GO (2004) Convection driven by differential heating at a horizontal boundary. J Fluid Mech 516:181–209

Paparella F, Young WR (2002) Horizontal convection is non-turbulent. J Fluid Mech 466:205–214

Pierce DW, Rhines PB (1996) Convective building of a pycnocline: laboratory experiments. J Phys Oceanogr 26:176–190

Pope SB (2000) Turbulent Flows. Cambridge University Press

Rossby T (1965) On thermal convection driven by non-uniform heating from below: an experimental study. Deep-Sea Res 12:9–16

Rossby T (1998) Numerical experiments with a fluid heated non-uniformly from below. Tellus 50A:242–257

Sandström JW (1908) Dynamische versuche mit meerwasser. Annalen der Hydrographic und Maritimen Meteorologie 36:6–23

Schmittner A (2005) Decline of the marine ecosystem caused by a reduction in the atlantic overturning circulation. Nature 434:628–633

Sharqawy MH, V JHL, Zubair SM (2010) Thermophysical properties of seawater: a review of existing correlations and data. Desalination and Water Treatment 16:354–380

Stewart KD, Hughes GO, Griffiths RW (2012) The role of turbulent mixing in an overturning circulation maintained by surface buoyancy forcing. J Phys Oceanogr 42:1907–1922

Stull RB (1988) An introduction to boundary layer meteorology. Kluwer Academic Publishers

Thielicke W (2014) The flapping flight of birds – analysis and application. PhD thesis, Rijksuniversiteit Groningen

Toggweiler JR, Samuels B (1997) On the ocean's large-scale circulation near the limit of no vertical mixing. J Phys Oceanogr 28:1832–1852

Vellinga M, Wood RA (2002) Global climatic impacts of a collapse of the atlantic thermohaline circulation. Climatic Change 54:251–267

Vreugdenhil CA, Hogg AM, Griffiths RW, Hughes GO (2016) Adjustment of the meridional overturning circulation and its dependence on depth of mixing. J Phys Oceanogr 46:731–747

Wang W, Huang RX (2005) An experimental study on thermal circulation driven by horizontal differential heating. J Fluid Mech 540:49–73

Westerweel J, Scarano F (2005) A universal detection criterion for the median test. Exp in Fluids 39:1096–1100

Whitehead JA, Wang W (2008) A laboratory model of vertical ocean circulation driven by mixing. American Meteorological Society 38:1091–1106

Wunsch C (2005) The total meridional heat flux and its oceanic and atmospheric partition. J Climate 18:4374–4380

Wunsch C, Ferrari R (2004) Vertical mixing, energy, and the general circulation of the ocean. Annu Rev Fluid Mech 36:281–314